ORIGINAL ARTICLE

Estimation of flexible needle deflection in layered soft tissues with different elastic moduli

Hyosang Lee · Jung Kim

Abstract The estimation of needle deflection when the needle interacts with biological tissue is challenging in needle steering. Most previous studies have used homogeneous tissue models to estimate the deflection of a needle. However, biological tissue typically has a layered structure with variable mechanical properties and geometric features. In this study, we propose a needle deflection model with a double-layered elastic medium. Each layer possesses distinct mechanical properties, which result in inconsistent degrees of friction force on the needle surface, needle-cutting force, and forces caused by the stiffness of the elastic medium. The model uses the Rayleigh–Ritz method to analytically estimate the needle deflection. To validate the model, needle steering experiments were performed using double-layered tissue phantoms and porcine tissues. The experimental results revealed that changes in reaction force at the needle base occurred when the needle passed through the boundary between the two layers. The mean absolute error between the estimated and measured needle tip trajectory was 0.88 ± 0.30 mm for the double-layered tissue phantom and 1.85 ± 0.73 mm for the porcine tissue. These results are comparable with previous studies of homogeneous tissue. The proposed model could improve needle steering in biological tissues, which consist of multiple layers.

Keywords Needle steering · Needle deflection model · Layered soft tissue

H. Lee · J. Kim (✉)
Division of Mechanical Engineering, School of Mechanical, Aerospace and Systems Engineering, Korea Advanced Institute of Science and Technology, Daejeon, Republic of Korea
e-mail: jungkim@kaist.ac.kr

H. Lee
e-mail: ginogino@kaist.ac.kr

1 Introduction

Needle steering is a promising technique in medical procedures such as needle ablation, needle biopsy, and brachytherapy [14, 19, 22]. Estimating the flexible needle deflection is a key technique for improving the accuracy of needle placement because the deflection can be used to estimate the trajectory of the needle to reach the specified anatomical regions [6].

Many studies have suggested the analytical needle deflection model with a homogeneous elastic medium. Although finite element-based models have produced accurate estimations of needle deflection and soft tissue deformation, their long computation time was not ideal for the real-time servo loop control of needle steering [7, 9]. Kataoka et al. [12] modeled needle deflection as a function of the resistance force caused by the stiffness of the soft tissue. The resistance force was described as a virtual spring in the lateral direction by Glozman et al. [10]; however, the components of the resistance force were not identified. Based on needle insertion experiments, Okamura et al. [17] identified three components of the resistance force. These components were the friction force applied to the needle shaft, the tissue-cutting force applied to the needle tip, and the force caused by the stiffness of the soft tissue. These needle–tissue interaction forces have been included in models of needle deflection. Misra et al. [16] calculated needle deflection using an energy-based formulation with the Rayleigh–Ritz method to incorporate the needle–tissue interaction forces. Asadian et al. [2] calculated needle deflection using the Euler–Bernoulli beam theory with force equilibrium. They improved the friction force model by considering dynamic friction. According to Cowan et al. [6], aforementioned needle deflection models in
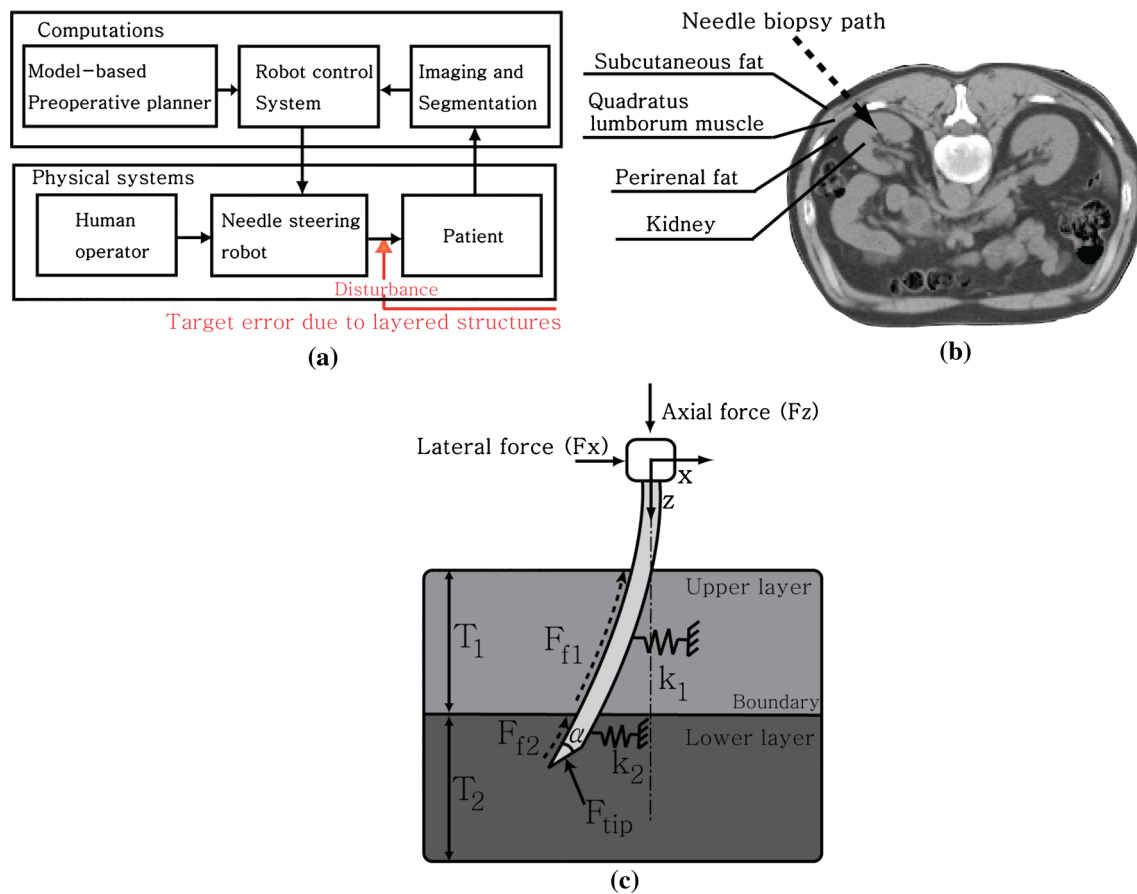
Fig. 1 **a** Diagram of the medical image guided needle steering system combining computations and physical systems [6], **b** needle insertion into layered soft tissue for a kidney biopsy, and **c** a needle steering model for double-layered soft tissues with different elastic moduli (E_1, E_2), friction forces (F_{f1}, F_{f2}), and thicknesses (T_1, T_2)

homogeneous soft tissue have been used with medical imaging as shown in Fig. 1a. The success of these medical image guided needle steering systems needs both computational and physical system. A needle deflection model is extensively used to produce desired trajectory in preoperative planner and is also used to control the needle steering system. Medical imaging is used as a feedback loop to steer the needle. Most of the needle steering systems assume the soft tissue as a homogeneous tissue.

However, biological tissue exhibits inhomogeneity, non-linear viscoelasticity, and anisotropy in general. A needle can penetrate several layers of skin, muscle, fatty tissue, and connective tissue to reach the target organ, as shown in Fig. 1b. These layers each have distinct mechanical properties, which affect needle deflection in terms of the tissue-cutting force, the friction force, and the force caused by the stiffness of each layer [3, 5, 15]. These factors are working as a disturbance as shown in Fig. 1a. Although medical images can be used to minimize the disturbance in needle steering systems with a needle deflection model in homogeneous tissues, it can fail to modify the trajectory of the

needle. This situation can be dangerous for some clinical cases in terms of bleeding such as liver biopsy [22] and kidney biopsy [14].

Despite the importance of the needle deflection model in layered soft tissues, little attention has been paid to the analytical model of needle deflection in layered soft tissues. Yan et al. [26] proposed an analytical needle deflection model in layered tissue using a depth-varying virtual spring and damper with online parameter estimation. They performed the needle steering experiments on a double-layered tissue phantom that consisted of a gelatin phantom and porcine meat. However, their model considered neither the friction force nor the tissue-cutting force, which are major factors in needle–tissue interaction forces.

To examine the consequences of the boundary formed between two layers, we presented a needle deflection model of a double-layered soft tissue with inconsistent needle–tissue interaction forces. This model was composed of the friction applied to the needle shaft, the needle tip force applied to the needle tip, and the force caused by the stiffness of the

soft tissue, as shown in Fig. 1c. The Rayleigh–Ritz energy method was used to estimate the deflection. Needle steering experiments were performed on homogeneous tissue phantoms, double-layered tissue phantoms with different elastic moduli and thicknesses, and porcine tissue that contained skin and muscle layers. The needle tip trajectory was estimated and compared with the measured needle tip trajectory to validate the proposed model. This study extended previous needle deflection models from homogeneous tissues to double-layered tissues.

2 Methods and materials

The mathematical formulation to calculate needle deflection for double-layered soft tissue will be introduced in the first section. Then, experimental setups of the needle steering system and the layered soft tissues will be introduced in the second section.

2.1 Needle deflection model for double-layered soft tissue

The deflection of a needle is closely related to the interaction forces between the needle and soft tissues because the needle could be modeled as a thin cantilever beam. The proposed needle deflection model used the Rayleigh–Ritz method to analytically calculate needle deflection [1, 16]. This model has three assumptions. First, each step of the estimation is in a quasi-static state because the needle steering velocity is as low as 0.1 mm sec^{-1}. Second, the stiffness of the soft tissue is modeled as a linear spring, which is perpendicular to the direction of insertion due to the small displacement of deformation between the needle and soft tissue. Third, the effect of soft tissue relaxation can be neglected because this effect is less than 5 % of the maximum force.

For the flexible needle and deformable soft tissue system, the entire energy of the system $\Lambda_{\text{total}}^{(i)}$ is calculated as follows:

$$\Lambda_{\text{total}}^{(i)} = \Lambda_{\text{bend}}^{(i)} + \Lambda_{\text{interact}}^{(i)} - \Lambda_{\text{work}}^{(i)} \tag{1}$$

where $\Lambda_{\text{bend}}^{(i)}$ is the strain energy of the flexible needle of the i-th step, $\Lambda_{\text{interact}}^{(i)}$ is the strain energy of the elastic medium, and $\Lambda_{\text{work}}^{(i)}$ is the work performed by external forces, which are the friction force applied to the needle shaft and the tissue-cutting force applied to the needle tip. For the entire length of the needle, $\Lambda_{\text{bend}}^{(i)}$ is defined as follows

$$\Lambda_{\text{bend}}^{(i)} = \frac{EI}{2} \sum_{z=0}^{L} \left(\frac{d^2 v^{(i)}(z)}{dz^2} \right) \Delta z \tag{2}$$

where $v^{(i)}(z)$ is the deflection of the needle at the i-th time interval, E is the elastic modulus of the needle, I, the second

moment of inertia of the needle in the cross-sectional direction, z is the axial distance from the base of the needle, Δz is the length of the discretized element of the needle shaft, and L is the needle length as shown in Fig. 2a.

The sum of the energy stored in the elastic medium due to the deformation ($\Lambda_{\text{interact}}^{(i)}$) is a function of the stiffness per unit length of each elastic medium and the distance between the i-th position of the needle shaft and the position of the needle tip trajectory along the axial distance from the needle. This distance is denoted as X_k in Fig. 2a. Using X_k and the stiffness of the soft tissue (k_1, k_2), the strain energy of the elastic medium is defined as follows

$$\Lambda_{\text{interact}}^{(i)} = \sum_{z=T_0}^{T_0+T_1} \frac{1}{2} k_1 (X_k(z))^2 \Delta z + \sum_{z=T_0+T_1}^{L} \frac{1}{2} k_2 (X_k(z))^2 \Delta z \tag{3}$$

where T_0 denotes the distance between the needle base and the upper tissue surface, and T_1 denotes the thickness of the upper tissue layer. The sum of the energy from the external force ($\Lambda_{\text{work}}^{(i)}$) is defined as follows

$$\Lambda_{\text{work}}^{(i)} = \Lambda_{\text{axial}}^{(i)} + \Lambda_{\text{lateral}}^{(i)} \tag{4}$$

In classical cantilever mechanics, when the static axial force $F_z(z)$ is applied to the beam, the strain energy (Λ_{axial}) in the beam is defined as follows

$$\Lambda_{\text{axial}}^{(i)} = \sum_{z=0}^{L} \frac{F_z^{(i)}(z)}{2} \left(\frac{dv^{(i)}(z)}{dz} \right)^2 \Delta z \tag{5}$$

where $F_z^{(i)}(z)$ denotes the axial force distribution, as shown in Fig. 2b.

When the needle is inserted into the layered soft tissue, the needle–tissue interaction forces in the axial direction can be divided into two components according to the axial distance from the base, z in Fig. 2b. One component is the friction force applied to the shaft of the needle, which is caused by the contact with the layered tissue, and the other component is the tissue-cutting force, which is related to the fracture toughness of the soft tissue and the stiffness, which results in the force applied to the needle tip [11, 15]. In this model, the friction force was separated according to the layer of the soft tissue. Although the needle shaft friction has been known to be related to the relative velocity of the needle and the tissue [17], the friction per unit length was assumed to be constant in this model because the needle was inserted at a constant velocity. The following mathematical formula was used to calculate the axial force distribution:

Fig. 2 a Force equilibrium of discretized needle segments at the *i*-th step. The enlarged view of the needle segment shows the friction force exerted on the needle shaft (F_{f1}) and the force caused by the stiffness of the soft tissue (F_{k1}). **b** The axial force distribution ($F_z^{(i)}(z)$) at the i-th step. The function includes the axial-directional component of the friction forces due to each layer (F_{f1}, F_{f2}) and the asymmetric tip force (F_{tip})

(a)

(b)
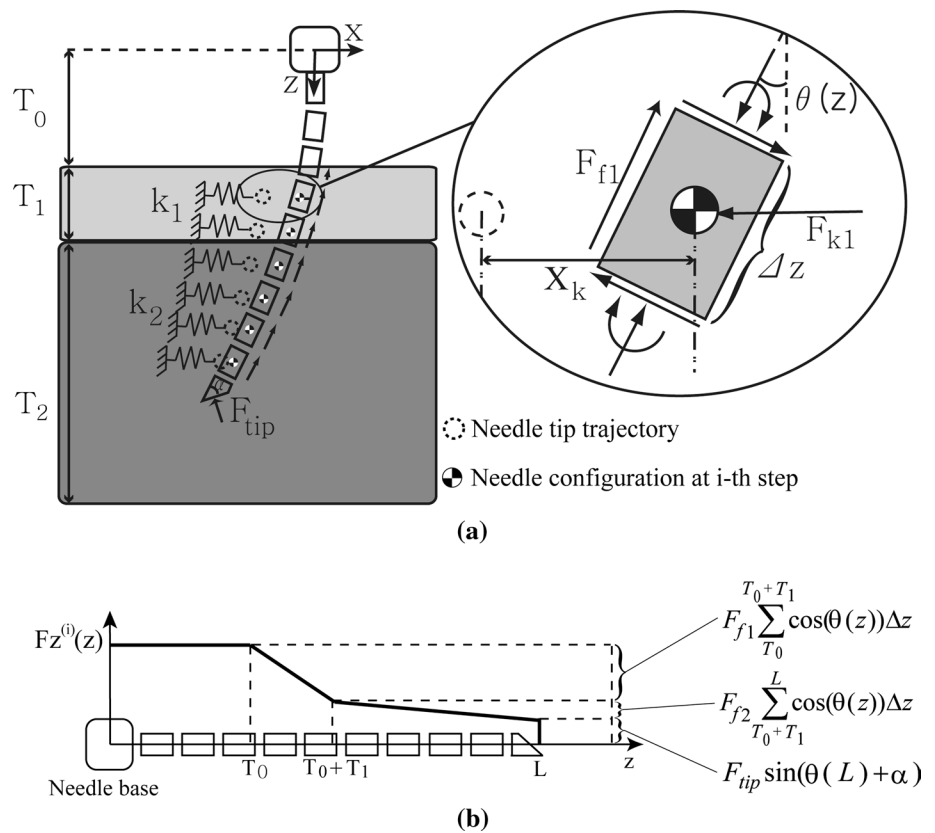
$$
F^{(i)}(z) = \begin{cases} F_{f1} \sum_{\hat{z}=T_0}^{T_0+T_1} \cos(\theta^{(i-1)}(\hat{z}))\Delta z + F_{f2} \sum_{\hat{z}=T_0+T_1}^{L} \cos(\theta^{(i-1)}(\hat{z}))\Delta z + F_{tip}\sin(\theta^{(i-1)}(L)+\alpha), & z < T_0 \\ F_{f1} \sum_{\hat{z}=z}^{T_0+T_1} \cos(\theta^{(i-1)}(\hat{z}))\Delta z + F_{f2} \sum_{\hat{z}=T_0+T_1}^{L} \cos(\theta^{(i-1)}(\hat{z}))\Delta z + F_{tip}\sin(\theta^{(i-1)}(L)+\alpha), & T_0 < z < T_0+T_1 \\ F_{f2} \sum_{\hat{z}=z}^{L} \cos(\theta^{(i-1)}(\hat{z}))\Delta z + F_{tip}\sin(\theta^{(i-1)}(L)+\alpha), & T_0+T_1 < z < L \\ F_{tip}\sin(\theta^{(i-1)}(L)+\alpha), & z = L \end{cases}
$$

(6)

where α is the bevel angle of the needle tip, F_{tip} is the cutting force exerted on the needle tip, F_{f1} is the friction force per unit length of the upper tissue layer, F_{f2} is the friction force per unit length of the lower tissue layer, and $\theta^{(i)}(z)$ is the angle between the needle shaft and the *z*-axis.

The energy in the lateral direction, $\Lambda_{lateral}^{(i)}$, depends on the work done by the friction force and the force exerted on the needle tip.

$$
\Lambda_{lateral}^{(i)} = \sum_{z=T_0}^{T_0+T_1} F_{f1}\sin(\theta^{(i-1)}(z))(v^{(i)}(z) - v^{(i-1)}(z))\Delta z
$$

$$
+ \sum_{z=T_0+T_1}^{L} F_{f2}\sin(\theta^{(i-1)}(z))(v^{(i)}(z) - v^{(i-1)}(z))\Delta z
$$

$$
+ F_{tip}\cos(\theta^{(i-1)}(L)+\alpha)(v^{(i)}(L) - v^{(i-1)}(L)) \quad (7)
$$

From these equations, the system potential $\Lambda_{total}^{(i)}$ is calculated for each time interval. The functional form of the needle deflection should be initially assumed in the

Rayleigh–Ritz method. We assumed the deflection of the needle $v^{(i)}(z)$ to be a third-order polynomial because a third-order polynomial is sufficient to model the deflection of a needle.

$$
v^{(i)}(z) = a_0^{(i)} + a_1^{(i)}z + a_2^{(i)}z^2 + a_3^{(i)}z^3 \tag{8}
$$

The coefficients are evaluated by minimizing the system potential $\Lambda_{total}^{(i)}$

$$
\frac{\partial \Lambda_{total}^{(i)}}{\partial a_j} = 0, \ j = 0, 1, 2, 3 \tag{9}
$$

From this equation, four equations are obtained for the coefficients of the deflections. The functional form of the needle deflection can be analytically calculated using the Rayleigh–Ritz method.

The estimation procedures for the trajectory of the needle tip are modified from the previous research [16, 20].
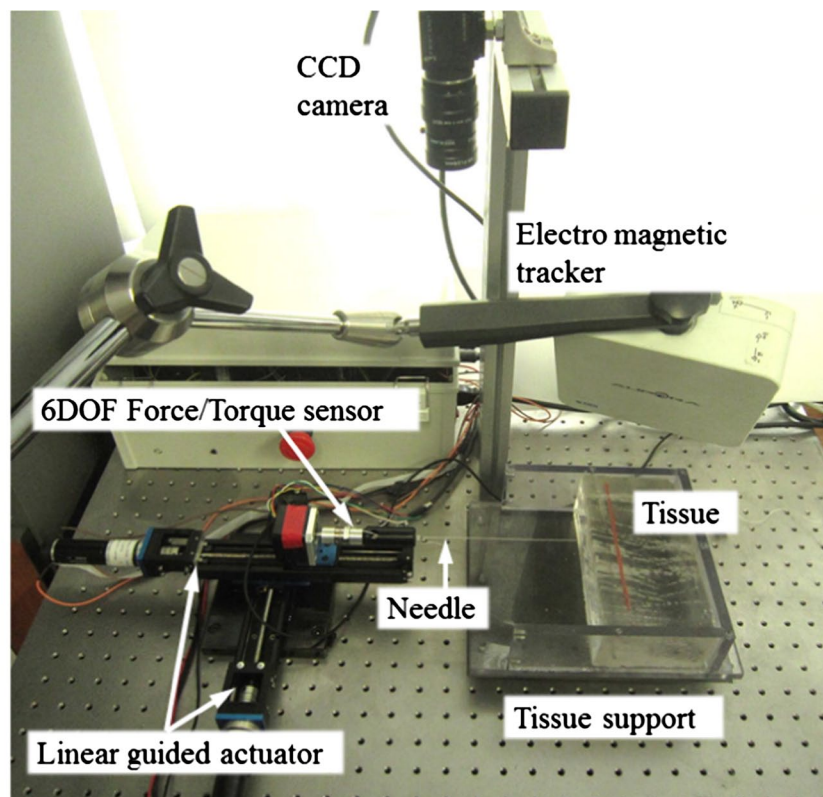
(a)
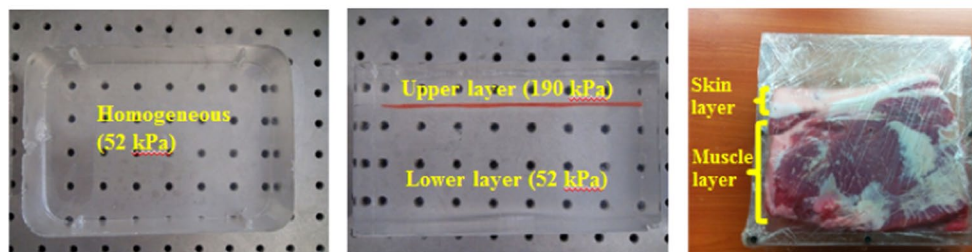
(b)

Fig. 3 **a** Two-dimensional needle steering system and **b** the homogeneous tissue phantom (*left*), one of the layered tissue phantoms (*middle*), and the porcine tissue, which contains skin and muscle layers (*right*)

This method estimated the needle insertions using discretized needle insertion steps with two sub-steps. At the first sub-step, the needle base is pushed into the elastic medium, and the axial and lateral reaction forces are measured from a force sensor located at the needle base. The axial forces consist of the friction force applied to the needle shaft and the tissue-cutting force applied to the needle tip, as defined in Eq. (6). Because the tissue-cutting force is difficult to model, it is calculated from the first sub-step. In the second sub-step, the configuration of the needle is calculated from the previous time interval to the i-th time interval using the needle deflection model. In our model, the first sub-step is modified to include the lateral movement of the needle base. This movement is denoted as X_k in Fig. 2a.

2.2 Experimental setups

Needle steering experiments were performed using a two-dimensional manipulator, as shown in Fig. 3a. The manipulator was designed to locate the needle base at the desired trajectory using two linear guided actuators (KR20, THK, Japan). The manipulator used a simple proportional integral derivative (PID) position control. A six degrees of freedom (DOF) force sensor (Nano17, ATI, USA) was attached between the linear guide and the base of the needle to measure the reaction forces. A 21-gauge Chiba needle (Aurora needle, Northern Digital, Canada) was firmly attached to the force sensor. This needle has a 0.8 mm diameter, 150 mm length, bevel angle of 24.8°, and

Table 1 Estimated parameters of needle–tissue interaction forces in tissue phantoms and porcine tissue [16, 20]

Tissue type (elastic modulus)	Factors affecting needle–tissue interaction forces		
	Friction per unit length (N mm^{-1})	Stiffness (N mm^{-1})	Force applied to the needle tip (N)
Tissue phantom (52 kPa)	0.0150 ± 0.0027	0.0200 ± 0.0011	0.1166 ± 0.0370
Tissue phantom (90 kPa)	0.0181 ± 0.0020	0.0311 ± 0.0020	0.1119 ± 0.0623
Tissue phantom (140 kPa)	0.0298 ± 0.0028	0.0482 ± 0.0021	0.1302 ± 0.0680
Tissue phantom (190 kPa)	0.0352 ± 0.0039	0.0725 ± 0.0016	0.2683 ± 0.1160
Porcine skin tissue (154 kPa)	0.0286 ± 0.0088	0.0661 ± 0.0044	0.3838 ± 0.2872
Porcine muscle tissue (58 kPa)	0.0141 ± 0.0057	0.0282 ± 0.0051	0.2320 ± 0.0748

elastic modulus of 200 GPa. A five DOF magnetic sensor coil (Aurora, Northern Digital, Canada) was integrated into the needle tip to track the needle tip trajectory. A camera (Flea2, Point Grey Research, USA) was installed on top of the system to capture the configuration of the needle.

A layered tissue phantom was constructed to have various mechanical properties and geometric features as shown in Fig. 3b. The mechanical properties of the subcutaneous skin, muscles, and internal organs were based on the literature [13, 21]. In this research, the double-layered tissue phantoms had elastic moduli of 90, 140, and 190 kPa for the upper layer and 52 kPa for the lower layer. The thickness of the upper layer was set from 5 to 25 mm in 5-mm intervals. For comparison, a homogeneous phantom of 52 kPa was also constructed using a silicone gel (DSE 7310, DLE 40, Dongyang Silicone, Korea). For the porcine tissue experiments, porcine tissue containing distinctive tissue layers was prepared. The layers consisted of the skin and muscle tissues. The thickness of the skin tissue layer was approximately 25 mm. An indentation test introduced by Egorov et al. [8] was used to obtain the elastic modulus of each layer of tissue, and the elastic moduli of the skin and muscle layers were found to be 154 and 58 kPa, respectively. The surface friction per unit length (F_{f1}, F_{f2}), the force applied to the needle tip (F_{tip}), and the stiffness of the tissue (k_1, k_2) of the tissue phantom and porcine tissue are obtained using the method introduced from the previous research [16, 20]. The surface friction per unit length is obtained after the needle fully penetrates the tissue. The force applied to the needle tip is calculated from the Eq. (6). The stiffness of the tissue is obtained from the compression test [16]. These parameters are presented in Table 1.

3 Experimental results

Needle steering experiments were performed to examine the consequences of the boundary formed between two layers, which affects the reaction force at the needle base and the needle tip trajectory. For each of the three tissues

(homogeneous, layered, and porcine), needle base manipulation with the same steering trajectory was performed ten times. The needle base was simultaneously driven 80 mm into the tissue in the axial direction with a velocity of 0.1 mm sec^{-1} and 20 mm in the lateral direction with a velocity of 0.025 mm sec^{-1}. At the initial insertion point, the needle was aligned perpendicular to the tissue surface to prevent misalignment. To minimize its movement, the soft tissue was immobilized by a tissue support, as shown in Fig. 3a. The needle base position, reaction forces, and needle tip position were recorded during the experiments. All of the experiments were performed and repeated at room temperature. The statistical method used was a one-way analysis of variance for nonparametric data also known as the Kruskal–Wallis test.

3.1 Tissue phantom study

Needle steering experiments were performed using the tissue phantoms to observe the reaction force responses and needle tip trajectories with respect to changes in the thickness and elastic modulus of the upper layer. Figure 4 presents the mean values of the axial forces (a) and lateral forces (b) measured from the force sensor for the homogeneous and layered tissue phantoms, which had elastic moduli of 90 kPa (top), 140 kPa (middle), and 190 kPa (bottom) in the upper layer. In Fig. 4a, although the material properties of the lower layer of the double-layered tissue phantoms and the homogeneous tissue phantoms were the same, the reaction force responses showed interesting features in terms of the slope change and the sudden reduction in the axial force when the needle tip passed through the boundary formed between the two layers. The slope change of the axial forces was calculated from the ratio of the slopes, which were obtained from the linear fitting of the axial forces. The percentages of the slope change of the axial force are presented in Table 2. To analyze the differences between the slope change and thicknesses or elastic moduli of the upper layer, a one-way analysis of variance for nonparametric data also known as the Kruskal–Wallis test was used. The slope change was significantly different with

Fig. 4 Experimental results representing **a** means and standard deviations of the axial forces of the double-layered tissue phantoms and porcine tissue experiments (*bottom*) and **b** means and standard deviations of the lateral forces of the double-layered tissue phantom and porcine tissue experiments (*bottom*)


(a)
(b)
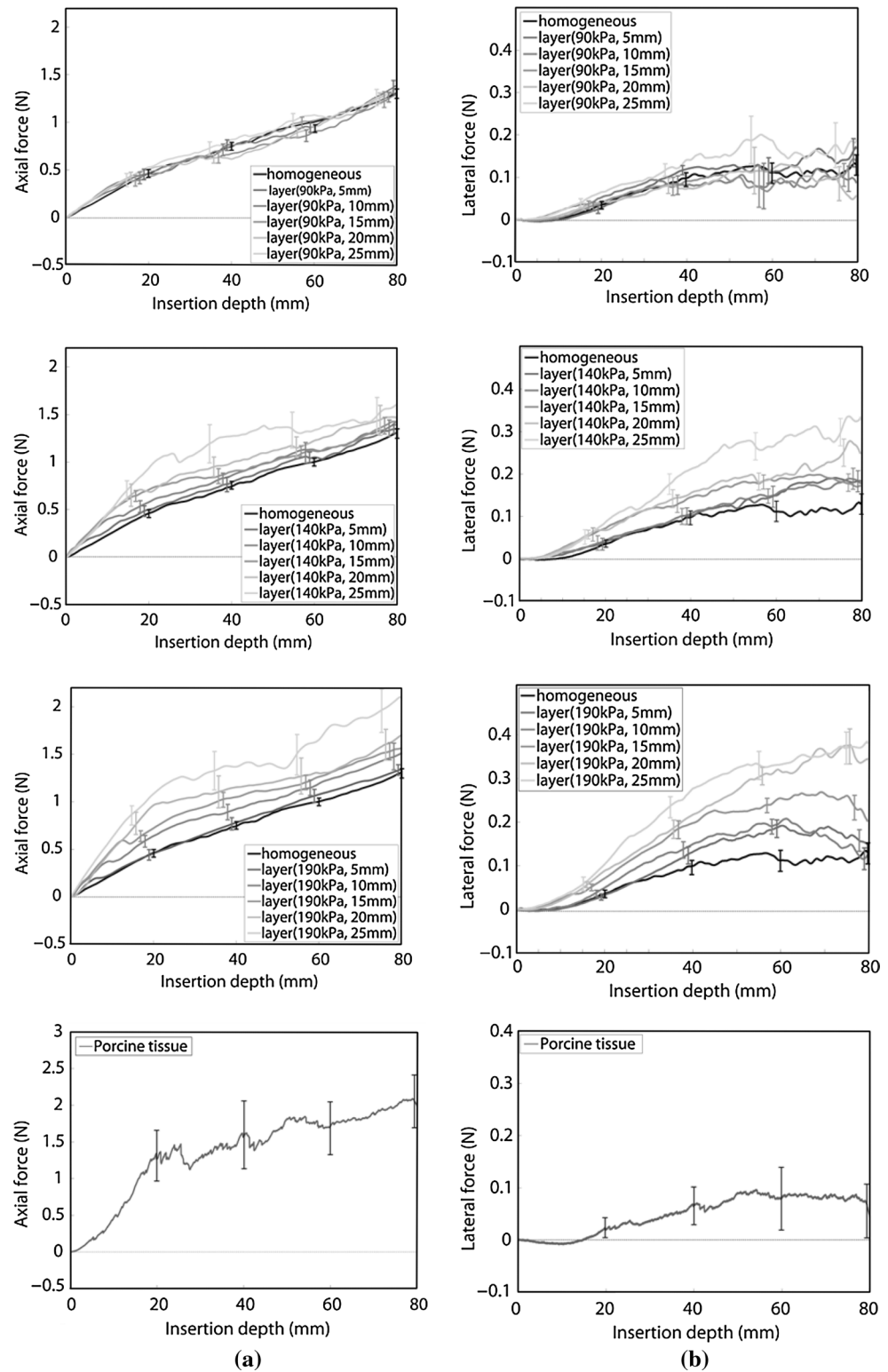
respect to the elastic modulus of the upper layer ($p < 0.001$). For the experiments performed with the 90, 140, and 190 kPa upper-layer tissue phantoms, the average slope change was 65, 53, and 44 %, respectively. In contrast, the slope change showed a smaller difference ($p = 0.09$) with

respect to the thickness of the upper-layer tissue than the elastic modulus of the upper-layer tissue. A sudden decrease in the axial force was also observed for the experiments performed with the 140 and 190 kPa upper-layer tissue phantoms, where the insertion depth was slightly farther from the

Table 2 Means and standard deviations of the rate of change in the slope of the axial force and the reduction in the axial force at the boundary formed between two layers and the final position of the needle tip

	Thickness of upper layer (mm)	Tissue type (elastic modulus of upper layer)				
		Tissue phantom (90 kPa)	Tissue phantom (140 kPa)	Tissue phantom (190 kPa)	Porcine tissue (154 kPa)	Homogeneous tissue (52 kPa)
Rate of change in the slope of the axial force (%)	5	84.42 ± 14.78	65.75 ± 5.73	48.18 ± 6.68	22.54 ± 42.61	–
	10	40.36 ± 10.86	43.29 ± 16.18	60.00 ± 10.55		
	15	62.44 ± 17.54	43.61 ± 29.12	39.63 ± 17.48		
	20	64.91 ± 8.41	58.76 ± 11.60	32.46 ± 11.66		
	25	73.07 ± 16.95	58.05 ± 7.45	44.28 ± 22.18		
Reduction in force at the boundary (N)	5	0.017 ± 0.038	0.008 ± 0.012	0.006 ± 0.003	0.327 ± 0.135	–
	10	0.035 ± 0.012	0.022 ± 0.026	0.018 ± 0.013		
	15	0.023 ± 0.005	0.028 ± 0.034	0.031 ± 0.024		
	20	0.034 ± 0.021	0.026 ± 0.007	0.017 ± 0.008		
	25	0.051 ± 0.091	0.072 ± 0.021	0.089 ± 0.126		
Final needle tip position (mm)	5	8.81 ± 1.35	10.46 ± 1.45	9.73 ± 1.50	14.70 ± 3.54	9.15 ± 1.44
	10	8.83 ± 1.77	11.72 ± 2.05	12.87 ± 2.96		
	15	10.12 ± 2.62	14.01 ± 3.04	13.51 ± 3.35		
	20	9.04 ± 2.31	14.68 ± 3.90	16.31 ± 3.76		
	25	11.55 ± 2.85	16.14 ± 4.23	17.36 ± 4.82		

Fig. 5 Experimental results representing the means and standard deviation of the needle tip positions of the double-layered tissue phantoms and porcine tissue experiments
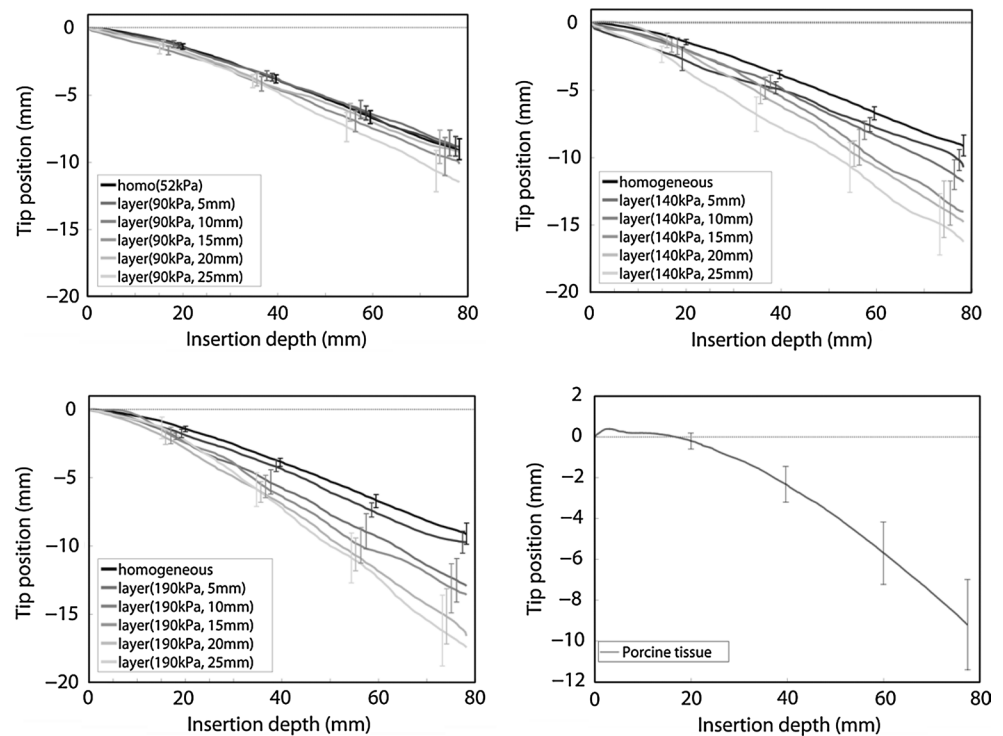
boundary formed between two layers. Table 2 presents the amounts of the sudden reductions in the axial forces. The differences between these sudden reductions and the thickness of the upper layer were significant ($p < 0.001$). However, the sudden reductions and the elastic modulus of the upper layer showed no significant difference ($p = 0.284$).

Although slope changes were observed in the axial force, relatively small changes in the slope were observed in the lateral force relative to the axial force responses, as shown in Fig. 4b. Furthermore, the rate of increase in the axial forces was reduced with respect to the needle insertion depth from 0 mm to the boundary formed between

the two layers in Fig. 4a; however, the rate of increase in the lateral forces increased with respect to same insertion depth. After the needle tip passed through the boundary, the rate of increase in the lateral force decreased.

Figure 5 presents the mean values of the trajectories of the needle tip in the homogeneous and layered tissue phantom experiments. Interestingly, no significant changes were observed in the trajectories of the needle tip when it passed through the boundary formed between the two layers. In Table 2, the amounts of deviation of the final needle tip position with respect to the elastic modulus and thickness of the upper layer are presented. As the thickness of the upper layer increased, the amount of deviation of the final needle tip position increased ($p < 0.001$). The increase in the elastic modulus of the upper layer was also significantly different from the increase in the amount of deviation of the final needle tip position ($p < 0.001$).

3.2 Porcine tissue study

To evaluate the proposed model in biological tissues, the needle base manipulation with the same steering trajectory as in the tissue phantom study was performed on porcine tissue. Figure 4a shows means and standard deviations of the axial force (bottom), Fig. 4b shows means and standard deviations of the lateral force (bottom), and Fig. 5 shows means and standard deviations of the needle tip trajectory in porcine tissue. Although a relatively large amount of fluctuation was observed in the force responses, distinct slope changes in the axial force were observed near the boundary between the skin and muscle layers. The slope changes of the axial force in the porcine tissue were larger than in the tissue phantom experiments, with 140 kPa ($p = 0.022$) or 190 kPa ($p = 0.009$) in the upper layer. A distinct force reduction was also observed near an insertion depth of 25 mm. The decrease in the force was quite large compared with the tissue phantom experiments. The rate of the increase in the axial forces increased between insertion depths of 0 and 20 mm. In Fig. 4b, the lateral forces between insertion depths of 0 and 15 mm showed some negative values interestingly. The needle tip position moved slightly upward in the 0–20 mm insertion depth range. These discrepancies between the tissue phantom and porcine tissue experiments will be discussed in the next section.

4 Discussion

4.1 Analysis of the needle–tissue interaction forces

The needle–tissue interaction forces are the major factor that causes needle deflection. The influences of the thickness and elastic modulus of the upper layer on the

reaction force responses were assessed from the experimental results. The slope change was significantly different with respect to the elastic modulus of the upper layer of the tissue ($p < 0.001$); its difference with respect to the thickness of the upper layer of the tissue was less significant ($p = 0.09$). Based on previous research [17], the slope of the axial force is closely related to the friction per unit length applied to the needle shaft. This knowledge implies that a slope change results from a change in the friction per unit length. In our model, Eq. (6) evaluated this friction for double-layered tissue. From the results, the average slope changes were 65, 53, and 44 % for the experiments performed with the 90, 140, and 190 kPa upper-layer tissue phantoms, respectively. Compared with the friction per unit length presented in Table 1, the ratio of the friction per unit length decreased by 82, 50.3, and 42.6 % for the experiments performed with the 90, 140, and 190 kPa upper-layer tissue phantoms, respectively.

The rate of increase in the axial force decreased with respect to the needle insertion depth from 0 mm to the thickness of the upper layer. However, the rate of increase in the lateral force increased for the same insertion depth. These results are also consistent with the proposed model. In Fig. 2b, the cosine and sine of the friction component are applied to the needle base. The sum of the cosine and sine with respect to the shaft angle can be similar to the experimental results. However, according to the increase in the insertion depth, the lateral force decreases. This phenomenon is caused by a stiffness force in the lateral direction of the needle. As the insertion depth increases, the stiffness force also decreases in a negative direction. These results imply that the friction force applied to the needle shaft played an important role in the beginning; later, the stiffness force in the lateral direction became analogous to the friction force.

The sudden reduction in axial force is related to the change in the force applied to the needle tip, which consists of the tissue-cutting force and the stiffness force at the needle tip. It appears that the sudden change is mainly due to the tissue-cutting force because this change is observed when the needle tip passes through the upper-layer tissue. However, the sudden reductions and the elastic modulus of the upper layer showed no significant difference.

In the porcine tissue study, there were a few discrepancies between the results of the tissue phantom and porcine tissue experiments. These discrepancies may have been caused by different needle–tissue interaction behaviors, as reported in the literature [25]. The artificial phantoms tended to have higher friction per unit length values than the porcine tissues. As shown in Table 1, porcine tissue has a lower friction per unit length relative to the elastic modulus. The sudden drop in the axial force was more distinct in the porcine tissue than in the tissue phantom. This finding indicates

Fig. 6 Examples of estimated and measured trajectories of the needle tip from the double-layered tissue phantom (*left*) and porcine tissue experiments (*right*). The estimated tip position was calculated using the proposed needle deflection model
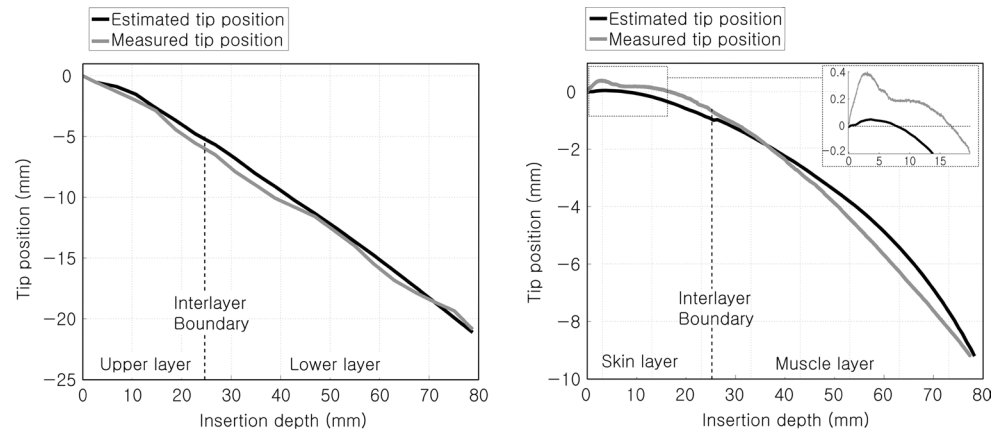
that the porcine tissue had a higher tissue-cutting force than the artificial phantoms. This different characteristic has also been previously reported [25]. For the porcine tissue, the boundary formed by the skin and muscle tissues was slightly altered along the insertion direction. This phenomenon was also consistent with previous research [11, 15], which reported that the rupture of the tissue is related to the fracture toughness of the soft tissue and the strain energy. Although the behavior of the tissue phantom and porcine tissue differed slightly, the overall trend of the axial and lateral force responses was similar with the tissue phantom study.

4.2 Comparison of estimation and experimental needle tip trajectories

Based on the experimental results, the elastic modulus and thickness of the upper layer were significantly different from the final tip trajectory. These results imply that the mechanical properties and geometry of the upper-layer tissue can influence the trajectory of the needle tip. Previous research has suggested a mechanical model of the needle deflection when the needle interacts with soft tissue in homogeneous soft tissues [2, 16]. The proposed model suggested the needle deflection model in layered soft tissue in an intuitive manner, and the needle tip trajectories were estimated to validate the proposed model.

Figure 6 presents examples of the estimation and experimental results of the needle tip trajectories for the tissue

phantom and porcine tissue experiments. As shown in Fig. 4a, there was an interesting absence of distinct changes when the needle tip passed through the boundary formed between the two layers, although sudden reductions in axial forces were observed in Fig. 4. In Fig. 6, changes were not observed in the estimated needle tip trajectory. It may be assumed that the lateral stiffness of the soft tissue absorbed the impact on the needle deflection caused by the sudden reduction in the axial force. There were discrepancies between estimated and measured tip position. These discrepancies came from the modeling error caused by the assumption of constant surface friction and tissue-cutting force. However, there was a research that showed that the friction force and tissue-cutting force slightly fluctuate with respect to the constant level [15]. This slight fluctuation causes modeling errors. These modeling errors resulted in the discrepancy between the estimated curves and measured curves.

The shape of the needle tip trajectory differed between the tissue phantom and porcine tissue experiments. The overall shape of the tip trajectory appeared to be a linear curve. However, the overall shape of the tip trajectory in the porcine tissue experiments appeared to be a circular arc. This difference is explained by the different needle–tissue interaction forces in the tissue phantom and the porcine tissue. As previously mentioned, friction force was a dominant factor in the needle–tissue interaction forces of the tissue phantom; however, the tissue-cutting force related to

Table 3 MAEs of the estimated trajectories of the needle tip compared with the experimental results

Tissue type	Elastic modulus of upper layer (kPa)	Thickness of upper layer				
		5 mm	10 mm	15 mm	20 mm	25 mm
Layered tissue phantoms	90	0.86 ± 0.30	0.78 ± 0.24	0.95 ± 0.38	0.62 ± 0.33	1.06 ± 0.37
	140	0.58 ± 0.24	0.64 ± 0.34	0.69 ± 0.29	0.50 ± 0.23	1.34 ± 0.64
	190	0.55 ± 0.23	0.73 ± 0.20	0.60 ± 0.33	1.48 ± 0.54	1.78 ± 0.84
Porcine tissue	154	1.85 ± 0.73				

the fracture toughness and stiffness of the soft tissue in the axial direction was a substantial factor in the needle–tissue interaction forces in the porcine tissue. The friction force was applied to the needle shaft; however, the tissue-cutting force was applied to the needle tip, which is analogous to bevel-tip needle steering [24]. The discrepancy between the estimated and measured trajectory was greater for porcine tissue experiments than tissue phantom experiments because the friction force and cutting force in porcine tissue are not well formulated due to tissue inhomogeneity and viscoelasticity.The mean absolute error (MAE) between the measured and estimated needle tip trajectories was calculated along the needle insertion depth using Eq. (10).

$$\text{MAE} = \frac{1}{N} \sum_{i=1}^{N} |P_{\text{estimated}}(i) - P_{\text{measured}}(i)| \qquad (10)$$

where $P_{\text{estimated}}$ is estimated needle tip position, P_{measured} is measured needle tip position, i is the discretized time interval, and N is total number of the intervals.

The overall errors are presented in Table 3. The MAE was 0.88 ± 0.30 mm for the double-layered tissue phantom experiments for ten replicates and 1.85 ± 0.73 mm for the porcine tissue experiments for ten cases. The estimation error of the porcine tissue experiments was higher than that of the tissue phantom experiments. This result may have been caused by the high fluctuation noise in the reaction force responses of the porcine tissue experiments. Although exact comparison is not possible due to the difference in experimental conditions, error of our work seems comparable with the previous models which have a MAE of 0.59 ± 0.3 mm for homogeneous tissue phantoms and 3.6 ± 1.85 mm for porcine tissues [16, 18, 23]. In the clinical aspect, acceptable limits are not defined; however, experienced physicians achieved targeting errors in the range of 5.5–6.5 mm [4]. Compared with this, we believe our model is clinically useful. Furthermore, our needle steering model can perform better when it is applied to the image guided needle steering system.

5 Conclusions

This study presents a needle deflection model in a double-layered elastic medium. This model considers the needle–tissue interaction forces, which are composed of the friction force applied to the needle shaft, tissue-cutting force, and the stiffness force caused by the elastic modulus of the tissue. Changes in the axial and lateral forces resulting from the layered composition of the tissue were observed during the needle steering experiments in the layered tissue phantoms and the porcine tissue. The presented model reflects these changes by accounting for the needle–tissue interaction forces, especially considering the layered structure of the soft

tissue. The MAE of the estimation of the needle tip trajectory was 0.88 ± 0.30 mm for the double-layered tissue phantom experiments and 1.85 ± 0.73 mm for the porcine tissue experiments which is comparable with the results obtained from the studies of homogeneous tissues. These results imply that the proposed model could be applied to needle steering for biological tissues with multiple layered structures.

References

1. Abayazid M, Roesthuis RJ, Reilink R, Misra S (2012) Integrating deflection models and image feedback for real-time flexible needle steering. Robot IEEE Trans 29(2):542–553
2. Asadian A, Kermani MR, Patel RV (2011) An analytical model for deflection of flexible needles during needle insertion. IEEE/RSJ international conference on intelligent robots and systems (IROS) 2551–2556
3. Barbe L, Bayle B, de Mathelin M, Gangi A (2007) In vivo model estimation and haptic characterization of needle insertions. Int J Robot Res 26(11–12):1283–1301
4. Blumenfeld P, Hata N, DiMaio S, Zou K, Haker S, Fichtinger G, Tempany C (2007) Transperineal prostate biopsy under magnetic resonance image guidance: a needle placement accuracy study. J Magn Reson Imaging 26(3):688–694
5. Carra A, Avila-Vilchis JC (2010) Needle insertion modeling through several tissue layers. 2nd International Asia Conference on Informatics in Control, Automation and Robotic*s* pp 237–240
6. Cowan NJ, Goldberg K, Chirikjian GS, Fichtinger G, Alterovitz R, Reed KB, Kallem V, Park W, Misra S, Okamura AM (2010) Robotic needle steering: design, modeling, planning, and image guidance. Surg Robot Syst Appl Vis 557–582
7. DiMaio SP, Salcudean SE (2003) Needle insertion modeling and simulation. IEEE Trans Robot Autom 19(5):864–875
8. Egorov V, Tsyuryupa S, Kanilo S, Kogit M, Sarvazyan A (2008) Soft tissue elastometer. Med Eng Phys 30(2):206–212
9. Elgezua I, Kobayashi Y, Fujie MG (2013) Survey on current state-of-the-art in needle insertion robots: open challenges for application in real surgery. Procedia CIRP 5:94–99
10. Glozman D, Shoham M (2007) Image-guided robotic flexible needle steering. IEEE Trans Rob 23(3):459–467
11. Gokgol C, Basdogan C, Canadinc D (2012) Estimation of fracture toughness of liver tissue: experiments and validation. Med Eng Phys 34(7):882–891
12. Kataoka H, Washio T, Audette M, Mizuhara K (2001) A model for relations between needle deflection, force, and thickness on needle penetration. Med Image Comput Comput Assist Interv 966–974
13. Levental I, Georges PC, Janmey PA (2007) Soft biological materials and their impact on cell function. Soft Matter 3(3):299–306
14. Mahal AS, Knauer M, Gregory PB (1981) Bleeding after liver biopsy. West J Med 134(1):11
15. Mahvash M, Dupont PE (2010) Mechanics of dynamic needle insertion into a biological material. IEEE Trans Biomed Eng 57(4):934–943
16. Misra S, Reed K, Schafer B, Ramesh K, Okamura A (2010) Mechanics of flexible needles robotically steered through soft tissue. Int J Robot Res 29(13):1640–1660

17. Okamura AM, Simone C, O'Leary MD (2004) Force modeling for needle insertion into soft tissue. IEEE Trans Biomed Eng 51(10):1707–1716

18. Patil S, Burgner J, Webster RJ, Alterovitz R (2014) Needle steering in 3-D via rapid replanning. IEEE Transactions on Robotics, Online publish

19. Phee SJ, Yang K (2010) Interventional navigation systems for treatment of unresectable liver tumor. Med Biol Eng Comput 48(2):103–111

20. Roesthuis RJ, van Veen YRJ, Jahya A, Misra S (2011) Mechanics of needle-tissue interaction. pp 2557–2563

21. Shergold OA, Fleck NA, Radford D (2006) The uniaxial stress versus strain response of pig skin and silicone rubber at low and high strain rates. Int J Impact Eng 32(9):1384–1402

22. Shidham GB, Siddiqi N, Beres JA, Logan B, Nagaraja H, Shidham SG, Piering WF (2005) Clinical risk factors associated with bleeding after native kidney biopsy. Nephrology 10(3):305–310

23. Vrooijink GJ, Abayazid M, Patil S, Alterovitz R, Misra S (2014) Needle path planning and steering in a three-dimensional non-static environment using two-dimensional ultrasound images. Int J Robot Res (in proof)

24. Webster RJ, Kim JS, Cowan NJ, Chirikjian GS, Okamura AM (2006) Nonholonomic modeling of needle steering. Int J Robot Res 25(5–6):509–525

25. Wedlick TR, Okamura AM (2012) Characterization of robotic needle insertion and rotation in artificial and ex vivo tissues. Biomedical Robotics and Biomechatronics (BioRob), 4th IEEE RAS & EMBS International Conference, pp 62–68

26. Yan KG, Podder T, Yan Y, Tien IL, Cheng CWS, Wan Sing N (2009) Tissue interaction modeling with depth-varying mean parameter: preliminary study. Biomed Eng IEEE Trans 56(2):255–262